The oxidation state and microstructural environment of transition metals (V, Co, and Ni) in magnetite: an XAFS study

Article *in* Physics and Chemistry of Minerals · May 2014

DOI: 10.1007/s00269-014-0727-4

Phys Chem Minerals (2015) 42:373–383
DOI 10.1007/s00269-014-0727-4

ORIGINAL PAPER

The oxidation state and microstructural environment of transition metals (V, Co, and Ni) in magnetite: an XAFS study

Xiaoliang Liang · Zisen He · Wei Tan · Peng Liu · Jianxi Zhu · Jing Zhang · Hongping He

Received: 27 July 2014 / Accepted: 3 December 2014 / Published online: 19 December 2014

Abstract Transition metal-substituted magnetite minerals have attracted increasing attention for their wide application in industry and environmental protection. In this study, the valence and atomic environment of some substituting metals in magnetites ($Fe_{3-x}M_xO_4$, M = V, Co, and Ni) were investigated using X-ray absorption fine structure spectroscopy. The results deduced from X-ray absorption near-edge structure spectroscopy indicated that the valences of V, Co, and Ni in $Fe_{3-x}M_xO_4$ were +3, +2, and +2, respectively. The valences did not change as the substitution extent increased. Extended X-ray absorption fine structure spectroscopy suggested that the substituting cations occupied octahedral sites in the magnetite structure. The M–O and M–M/Fe distances were consistent with the Fe_{oct}–O and Fe_{oct}–Fe distances, respectively, in the magnetite (Fe_3O_4) structure. The occupancy of the substituting cations was assessed by crystal-field theory. We also considered the relationship between the chemical environment of substituting cations and their effects on the physicochemical properties of magnetite, including thermal stability, surface properties, and catalytic reactivity.

Keywords Transition metal-substituted magnetite · XAFS · Oxidation state and structural environment · Crystal-field theory

Introduction

Transition metal-substituted magnetite minerals have received increasing attention due to their remarkable magnetic (Varshney and Yogi 2010), electrical (Kumari et al. 2014), and surface properties (Magalhaes et al. 2007). Having properties different from those of the bulk mineral, nanocrystalline magnetite is applicable for the fabrication of nanodevices, such as magnetic storage devices (Salazar-Alvarez et al. 2007), batteries (Zhu et al. 2013), and catalysts (Costa et al. 2006).

Magnetite, a member of spinel group minerals, has general formula of AB_2O_4, where A and B denote divalent and trivalent metal cations, respectively. The unit cell of spinel contains 32 oxygen atoms in a close-packed cubic arrangement, with 24 cations occupying 8 out of 64 available tetrahedral sites, and 16 out of 32 available octahedral sites. In the normal structure, represented by AB_2O_4, the A^{2+} cations occupy tetrahedral sites, while the B^{3+} cations occupy octahedral sites. In the inverse structure ($B[AB]O_4$), on the other hand, all the A^{2+} cations and one-half of the B^{3+} cations have exchanged site occupancy (Sickafus et al. 1999). Magnetite has an inverse structure, represented by $Fe^{3+}[Fe^{2+}Fe^{3+}]O_4$ where Fe^{2+} and one-half of Fe^{3+} occupy octahedral sites (Cornell and Schwertmann 2003).

In natural magnetite, divalent (Co, Ni, Zn, Cu, Mn, etc.), trivalent (Al, V, Cr, etc.), and tetravalent (Ti) cations

Electronic supplementary material The online version of this article (doi:10.1007/s00269-014-0727-4) contains supplementary material, which is available to authorized users.

X. Liang · Z. He · W. Tan · P. Liu · J. Zhu · H. He (✉)
Key Laboratory of Mineralogy and Metallogeny, Guangzhou Institute of Geochemistry, Chinese Academy of Sciences and Guangdong Provincial Key Laboratory of Mineral Physics and Materials, Guangzhou 510640, China
e-mail: hehp@gig.ac.cn

Z. He · W. Tan · P. Liu
University of Chinese Academy of Sciences, Beijing 100049, China

J. Zhang
Institute of High Energy Physics, Chinese Academy of Sciences, Beijing 100049, China

can isomorphously substitute for iron cations without changing the inverse spinel structure (Dupuis and Beaudoin 2011). By altering the valence and distribution of cations in octahedral and tetrahedral sites, isomorphous substitution can tune the physicochemical properties of magnetite. The magnetic property of magnetite arises from the super exchange of Fe^{3+} cations between octahedral and tetrahedral sites, while the conductivity is closely related to the charge ordering of Fe^{3+}–Fe^{2+} in octahedral sites (Cornell and Schwertmann 2003; Ounnunkad et al. 2006). The variation in cation distribution by Co and Ni incorporation affects the particle size and magnetic properties of magnetite (e.g., curie transition temperature) (Sorescu et al. 2002; Brabers et al. 1998). The influence of cation distribution also extends to the surface reactivity of magnetite as manifested by catalyzing Fenton-like reaction (Oliveira et al. 2004), persulfate activation (Su et al. 2013), and heavy metal transformation (Latta et al. 2013). The surface reactivity of magnetite is mainly associated with octahedral cations, rather than tetrahedral ones, because of the almost exclusive exposure of octahedral sites on the spinel surface (Ramankutty and Sugunan 2001). Substituting metals with thermodynamically favorable redox pairs (e.g., Mn^{2+}/Mn^{3+}, and Co^{2+}/Co^{3+}) also promote electron transfer during the reaction and hence enhance the reactivity of magnetite in catalyzing the advanced oxidation processes (Costa et al. 2006; Su et al. 2013) and heavy metal oxidation-reduction (Latta et al. 2013). Thus, the physicochemical properties of magnetite can be tailored by means of partial or complete substitution of divalent or trivalent iron by foreign cations in the spinel structure.

From the previous studies, the distribution and local environment of iron and substituting cations in magnetite structure have been investigated by a number of instrumental techniques, including X-ray diffraction (XRD) (Sorescu et al. 2001), thermogravimetry (TG) (Kester et al. 1996), X-ray photoelectron spectroscopy (XPS) (Kester et al. 1996), Mössbauer spectroscopy (Costa et al. 2003), and Fourier transform infrared spectroscopy (FTIR) (Nohair et al. 1995). XRD, however, is not suited for assessing structural changes because of the similarity in scattering factors and ionic radii between Fe and common substituting metals. In addition, nanosize particles give rise to broad XRD peaks. TG can be used to measure the loss or gain of structural oxygen under heating. But this method is not element-specific in that it cannot determine which of several possible ions are being oxidized or reduced during heating. Also, XPS just focuses on the surface chemical structure. Although FTIR and Mössbauer spectroscopy can probe the coordination environment of Fe cations, they could not precisely reflect the structural information with respect to the substituting cations.

Being composed of X-ray absorption near-edge structure (XANES) and extended X-ray absorption fine structure (EXAFS), X-ray absorption fine structure (XAFS) spectroscopy is a powerful technique for probing the chemical environment of atoms. XANES can provide information about the oxidation state and site symmetry of absorbing central atoms in mineral structure, while EXAFS can give insight into coordination numbers and distances of shells around such atoms (Peterson et al. 1997; Carta et al. 2007, 2008a). The occupancy of V, Mn, Cr, Co, and Ni has been investigated by distinguishing the intensity of the pre-edge peak on the XANES spectrum, as the intensity of pre-edge peak varies with the coordination symmetry (Liang et al. 2013b). For example, the pre-edge peak related to tetrahedral site should be obviously stronger than that of octahedral one, ascribed to its low symmetry. But the intensity change also varies with the degree of distortion from centrosymmetry in octahedral site (Waychunas et al. 1983). Therefore, uncertainty should exist in the analysis of occupancy by XANES. The application of EXAFS for investigating the atomic structure of magnetite has recently been developed. Liang et al. investigated the Fourier transform (FT) curves of EXAFS at V K-edge in vanadium-substituted magnetite (Liang et al. 2013a). However, the detail information of the V–V/Fe shells has not been presented, which provides very helpful information on the cation distribution in spinel structure. Carta et al. (Carta et al. 2008b) studied the inverse spinel structure in nanocrystalline $NiFe_2O_4$ by fitting the EXAFS data and indicated that all Ni^{2+} occupies octahedral sites and Fe^{3+} cations are equally distributed between tetrahedral and octahedral sites. But the effect of Ni content on the structure evolution has not been concerned. In this study, three series of transition metal-substituted magnetites ($Fe_{3-x}M_xO_4$, M = V, Co and Ni) were characterized by XAFS, with the main aim on the evolution of valence and chemical environment of substituting cations. Moreover, the occupancy of substituting cations was accessed by crystal-field theory (CFT) and utilized to discuss several experimental evidences about the effect of studied substitutions on the physicochemical properties of magnetite.

Materials and methods

All chemicals and reagents were of analytical grade and used as received. All the magnetite samples were synthesized by a precipitation–oxidation routine (Liang et al. 2010). The $Fe_{3-x}V_xO_4$ series of samples was obtained by dissolving a specified amount of $FeSO_4$ in a solution of HCl, adding 1.0 mL hydrazine, and keeping the pH at <1, in order to prevent the oxidation of ferrous cations and precipitation of iron hydroxide. After heating the

mixture at 90–100 °C, equal volumes of a solution containing 4.0 mol L^{-1} NaOH, 0.90 mol L^{-1} $NaNO_3$, and a predetermined amount of NH_4VO_3 were added drop wise (10 mL min^{-1}). The combined solution was kept at 90 °C for 5 h with stirring at a rate of 500 rpm and then allowed to cool at room temperature. At each step of the procedure, N_2 gas was passed through the system so as to prevent atmospheric oxidation of ferrous cations. The total concentration of Fe and V in the final solution was 0.45 mol L^{-1}. The mineral particles were separated by centrifugation at 3,500 rpm for 5 min, washed with boiling distilled water, and recentrifuged. After 3–4 more washings, the particles were dried in a vacuum oven at 100 °C for 24 h. Fe_3O_4 was obtained by following the above procedure without adding NH_4VO_3. The incorporation of Co and Ni into magnetite was achieved by dissolving pre-calculated amount of $CoCl_2$ and $NiSO_4$ in a solution of $FeSO_4$, but without adding NH_4VO_3. All the samples were ground and passed through a 200-mesh sieve.

The contents of Fe and substituting metals in the synthetic samples were determined on ICP-AES (Varian VISTA-PRO AX). Powder X-ray diffraction (PXRD) patterns were recorded between 10° and 80° (2θ) at a step of 1° min^{-1} on a Bruker D8 advance diffractometer with Cu $K\alpha$ radiation (40 kV and 40 mA). Specific surface areas (SSA) were measured by the adsorption of N_2 at 77 K, and applying the BET equation with correlation coefficient >0.999, using an ASAP 2020 instrument. The samples were degassed at 433 K for 12 h before measurement.

X-ray absorption fine structure (XAFS) spectra of the synthetic samples and reference compounds were measured on the beamline 1W1B of Beijing Synchrotron Radiation Facility (BSRF). The BSRF storage ring is operated at the electron energy of 2.2 GeV with beam current of 250 mA. The 1W1B is a focused X-ray beamline, using a Si (111) double-crystal monochromator. The beam size used at the sample position was about 900 × 300 μm^2. The K-edge spectra of V (5,465 eV), Co (7,709 eV), and Ni (8,333 eV) were acquired at room temperature in transmission mode using a Si (111) monochromator and an ion-chamber detector filled with 100 % N_2. X-ray 3*d* foil sets were used to perform energy calibration of the monochromator for all the target elements. The sample thickness was optimized to give an edge jump in the range of 0.6–1, depending on the content of the target element.

IFEFFIT software was used to sum the data, identify the beginning of the absorption edge, E_0, fit the pre- and post-edge backgrounds, and obtain the normalized absorbance χ as a function of the modulus of photoelectron wave vector k. Phase and amplitude functions for single-scattering paths were calculated using FEFF7. The backscattering amplitudes and phase shifts of the M–O and M–M/Fe wave functions were determined by fitting the reference samples. The structural parameters were obtained by nonlinear least-squares fitting in k space with a k^3 weighting to emphasize the high-energy part of the spectra. The fitting was carried out with the k range of 2.2–12.0 $Å^{-1}$ and the R range of 1.0–5.4 Å, at all the absorption edges. The quality of the fit was judged from the normalized sum of residuals. Reasonable fits on the EXAFS spectra have R-factor values <0.05.

Results and discussion

Chemical analysis and XRD

The chemical compositions of the synthetic $Fe_{3-x}M_xO_4$ (M = V, Co, Ni) samples are summarized in Table 1. The Fe content of the samples decreases as the V, Co, and Ni contents increase, implying that V, Co, and Ni have substituted for Fe in the structure of magnetites.

The XRD patterns (Fig. 1) of the V-, Co-, and Ni-substituted samples correspond closely to the standard reflections for magnetite (JCPDS: 19-0629) (Zhao et al. 2010), indicating that the synthetic samples have spinel structure. Some substitutions change the lattice parameter (a_0), crystal size, and SSA of magnetite (Table 1). The a_0 value is 8.411 Å for Fe_3O_4 magnetite, different from the literature

Table 1 Content in metal (C_M) and iron (C_{Fe}), lattice parameters, and specific surface area of synthetic magnetite samples $Fe_{3-x}M_xO_4$

Sample	C_M (%)	C_{Fe} (%)	a_0 (nm)	Crystal size (nm)	Specific surface area ($m^2 g^{-1}$)
Fe_3O_4	0	72.4	0.8411	28 (3)	28
$Fe_{2.84}V_{0.16}O_4$	3.6	68.7	0.8392	34 (3)	31
$Fe_{2.74}V_{0.26}O_4$	5.7	66.6	0.8408	35 (3)	26
$Fe_{2.66}V_{0.34}O_4$	7.7	64.6	0.8417	35 (3)	40
$Fe_{2.80}Co_{0.20}O_4$	5.0	66.6	0.8386	30 (3)	19
$Fe_{2.57}Co_{0.43}O_4$	10.7	60.6	0.8385	29 (3)	17
$Fe_{2.33}Co_{0.67}O_4$	16.6	54.7	0.8379	39 (3)	16
$Fe_{2.76}Ni_{0.24}O_4$	5.8	62.9	0.8382	25 (3)	39
$Fe_{2.52}Ni_{0.48}O_4$	11.1	55.3	0.8376	22 (3)	40
$Fe_{2.29}Ni_{0.71}O_4$	14.0	46.8	0.8372	24 (3)	49

C_M: The content of the substituting metals in magnetite, M = V, Co, and Ni

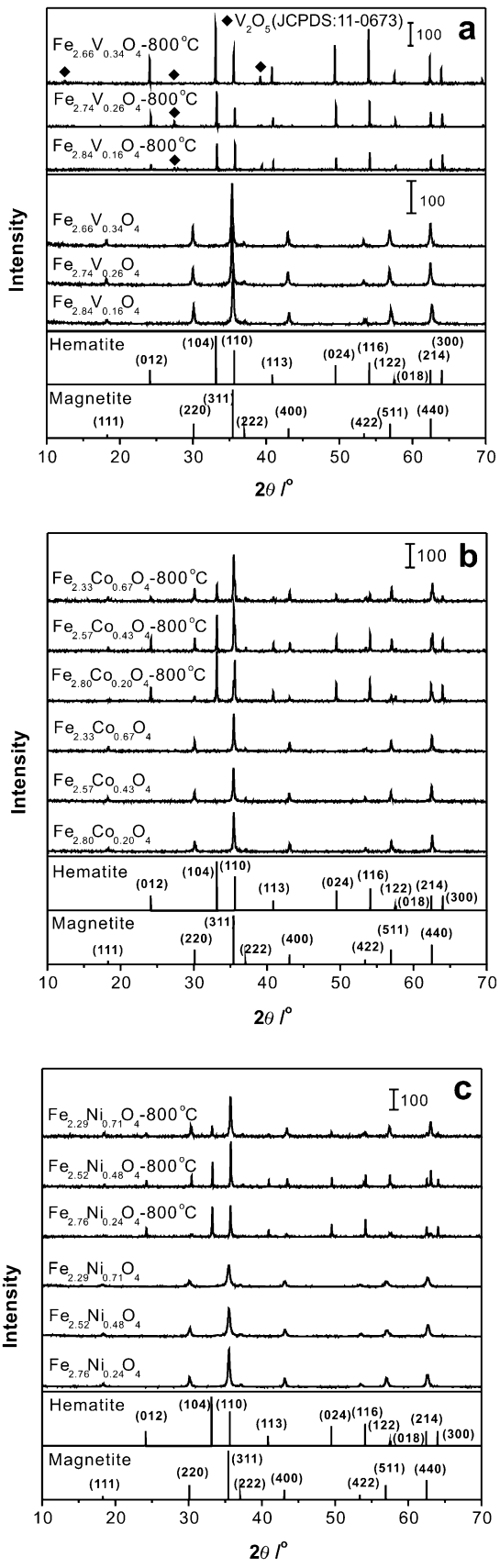

◀**Fig. 1** XRD patterns for synthetic $Fe_{3-x}V_xO_4$ (**a**), $Fe_{3-x}Co_xO_4$ (**b**), and $Fe_{3-x}Ni_xO_4$ (**c**) and their respective products after calcination at 800 °C for 3 h. The standard patterns for hematite and magnetite are also shown

a_0 value (8.391 Å), ascribed to the nanosize of particle. This phenomenon has been reported in the previous studies (Magalhaes et al. 2007; Pearce et al. 2012). The Ni substitution decreases crystal size, resulting in the broadening of XRD diffraction peaks. Moreover, the substitution of Ni gradually increases the SSA of magnetite, while the Co substitution show the decrease effect (Table 1).

XANES characterization

For the K-edge XANES spectra of V in $Fe_{3-x}V_xO_4$ and the reference samples (V_2O_3, VO_2, and V_2O_5), the pre-edge peak of V at about 5,470 eV is attributed to the transition from the bound-state 1*s* to 3*d* (Chen et al. 2002). The intensity of this peak decreases in the order $V_2O_5 > VO_2 > V_2O_3$ (Figs. 2a, 3a). In the case of V_2O_5, the presence of an empty *d*-orbital ($3d^0$) in vanadium atom increases the probability of 1*s*-to-3*d* transition, resulting in the high intensity of pre-edge peak. In V_2O_3, the existence of electrons in the *d*-orbital ($3d^2$) of vanadium atom and its central symmetry of nearest coordination shells (V–O) reduces the probability of 1*s*-to-3*d* transition and hence weaken the pre-edge peak. The intensity of the pre-edge peak for $Fe_{2.66}V_{0.34}O_4$ is comparable to that observed for V_2O_3, indicative of the regular alignment of the central vanadium atom.

Generally, the energy positions of the XANES spectra depend on the binding energy of the absorbing atom, and hence on the oxidation state, but also on other parameters, such as the nature and number of nearest neighbors (Pantelouris et al. 2004). A linear relationship between the edge shift and the valence state has been established for cations in samples with the nearest neighbors of the same chemical species. Based on this principle, the XANES spectra in this work were evaluated to investigate the valence of substituting metals in the synthetic samples, by comparing the spectra of the samples with each other, and with the spectra of reference compounds. The absorption edge is defined as the maximum of derivative at the absorption edge. The absorption K-edge at 5,480.2 eV for $Fe_{2.66}V_{0.34}O_4$ is close to the value for V_2O_3 but somewhat far from that for VO_2 and V_2O_5, suggesting that the valence of vanadium in $Fe_{2.66}V_{0.34}O_4$ is dominantly +3. The absorption edge of V shows two main peaks, denoted as P1 and P2 (Figs. 2a, 3a). For $Fe_{2.66}V_{0.34}O_4$, the main peak (P1) at 5,485.8 eV is stronger than that shown by the vanadium oxide reference samples. This observation may be ascribed to a decrease in static disorder of nearest neighbors, or an increase in the

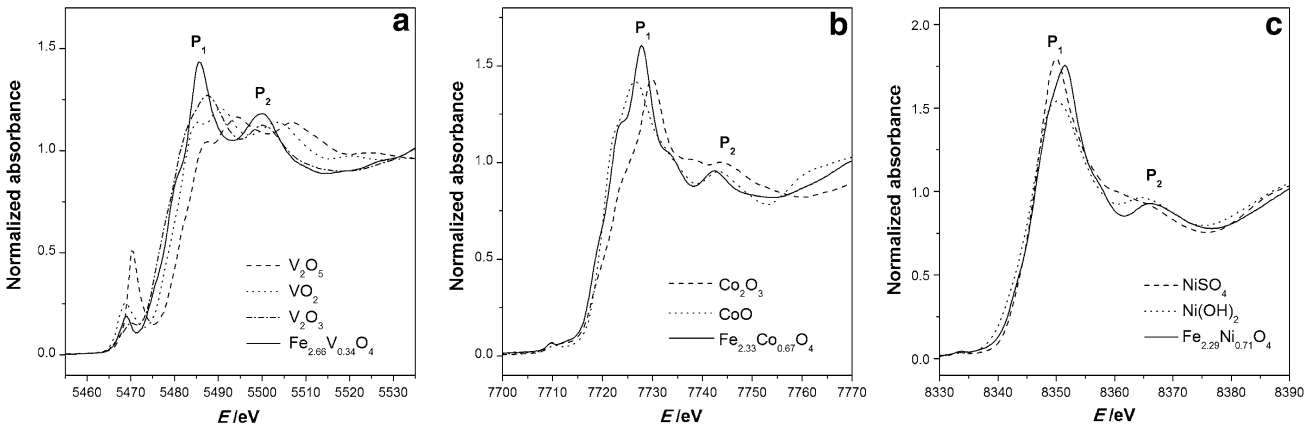

Fig. 2 K-edge XANES spectra of reference samples and $Fe_{2.66}V_{0.34}O_4$ (**a**), $Fe_{2.33}Co_{0.67}O_4$ (**b**), and $Fe_{2.29}V_{0.71}O_4$ (**c**)

coordination number of vanadium (Farges et al. 2001). The P2 peak for $Fe_{2.66}V_{0.34}O_4$ at 5,499.9 eV is also more pronounced as compared with the reference samples, probably because of the presence of regular and aligned V–V/Fe shells (Farges et al. 2001). The XANES spectra of $Fe_{3-x}V_xO_4$, however, do not noticeably vary as the V content increases.

For the $Fe_{3-x}Co_xO_4$ series, the pre-edge peak of Co is quite weak (Figs. 2b, 3d), indicating that the substituting cobalt cations largely exist in a high-spin arrangement, and the 1*s*-to-3*d* transition is forbidden. The absorption K-edges of cobalt in CoO, Co_2O_3, and $Fe_{2.33}Co_{0.67}O_4$ are at 7,718.2, 7,723.2, and 7,719.9 eV, respectively (Fig. 2b). The absorption K-edges for CoO and $Fe_{2.33}Co_{0.67}O_4$ are closely similar, indicating that the valence of cobalt in $Fe_{2.33}Co_{0.67}O_4$ is dominantly +2. The pronounced P2 peak for $Fe_{2.33}Co_{0.67}O_4$ implies the presence of a regular and aligned Co–Co/Fe shell. Like the vanadium-substituted series, the profiles of the $Fe_{3-x}Co_xO_4$ spectra do not change appreciably with the increase in Co content (Fig. 3d).

The absorption K-edge positions of nickel in the $NiSO_4$, $Ni(OH)_2$, and $Fe_{3-x}Ni_xO_4$ series (Figs. 2c, 3g) do not shift perceptibly, indicating that the valence of Ni in $Fe_{3-x}Ni_xO_4$ is mainly +2. The weak pre-edge peaks in the spectra of $Fe_{3-x}Ni_xO_4$ may be related to the low probability of 1*s*-to-3*d* transition for eight electrons in the *d*-orbital ($3d^8$) of Ni^{2+}. The intense P2 peak for the $Fe_{3-x}Ni_xO_4$ series (Fig. 3g) indicates the existence of regular and aligned Ni–Ni/Fe shells.

To check whether the substituting cations exist in the form of their corresponding amorphous metal hydro(oxides), or are incorporated into the spinel structure of magnetite, the synthetic samples were calcined at 800 °C in air for 3 h and then rapidly quenched. If the substituting cations exist as their amorphous hydro(oxides), the peaks related to their hydro(oxides) would appear on the XRD patterns of calcinated products. From the XRD peak intensity of the calcined samples (Fig. 1), calcination led to a sharpening of the peaks, suggesting that the heated samples are more crystallized than their untreated counterparts. In the case of the Ni- and Co-substituted series, calcination led to the formation of two main phases, identifiable with hematite and spinel ferrite (Fig. 1b, c). When unsubstituted magnetite is heated at about 200 °C in air, the ferrous ions in its structure are oxidized. As a result, the mineral is transformed into maghemite but the spinel structure is retained. The transformation of maghemite into hematite (at ~600 °C), however, leads to lattice rearrangement (Cornell and Schwertmann 2003). Thus, the presence of hematite would indicate the involvement of both oxidation and phase transformation. Since Ni^{2+} and Co^{2+} cannot be oxidized below 800 °C, they are retained in the spinel structure after the calcination, indicating that Ni and Co prefer to incorporate into the synthetic magnetite structure rather than exist as their (hydr)oxides. In the case of the vanadium-substituted ($Fe_{3-x}V_xO_4$) series, however, calcination led to the formation of hematite and V_2O_5 (Fig. 1a). The appearance of V_2O_5 is ascribed to the oxidation of V^{3+} cations at about 350 °C (Liang et al. 2010). As V^{5+} has a high valence and small cation radii, it cannot be accommodated in the spinel structure. A further survey was required to confirm the incorporation of vanadium into the magnetite structure.

EXAFS characterization

The EXAFS spectra for V_2O_3 and $Fe_{3-x}V_xO_4$ are shown in Fig. 3b, while the corresponding FT curves are displayed in Fig. 3c. In line with the XANES results, the profiles of the EXAFS spectra for $Fe_{3-x}V_xO_4$ samples are similar. This suggests that the atomic environment of vanadium in $Fe_{3-x}V_xO_4$ is closely similar. The first peak in the FT

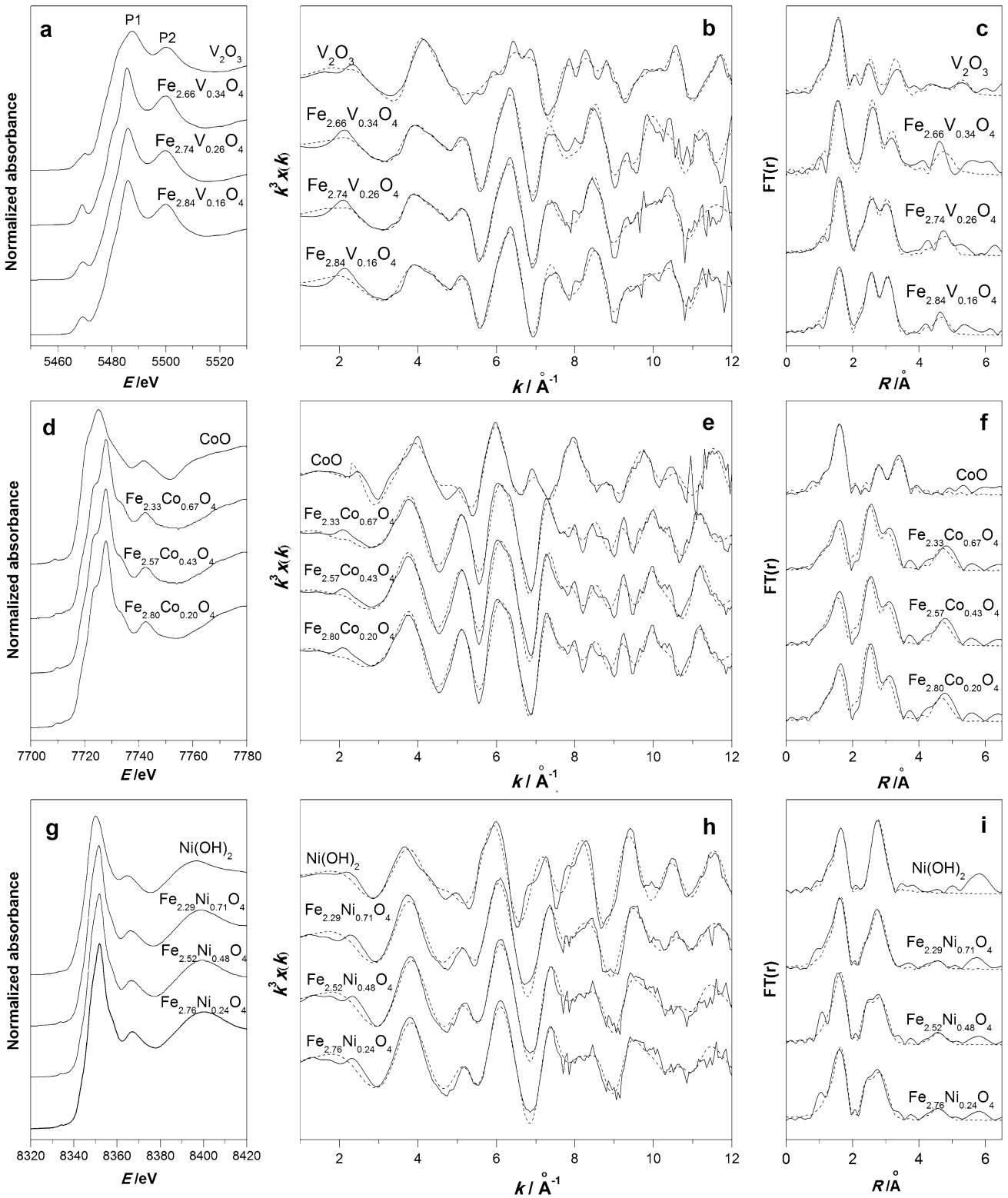

Fig. 3 K-edge XANES spectra for $Fe_{3-x}V_xO_4$ (**a**), $Fe_{3-x}Co_xO_4$ (**d**), and $Fe_{3-x}Ni_xO_4$ (**g**), together with the EXAFS spectra for $Fe_{3-x}V_xO_4$ (**b**), $Fe_{3-x}Co_xO_4$ (**e**), and $Fe_{3-x}Ni_xO_4$ (**h**) and the Fourier transform curves for $Fe_{3-x}V_xO_4$ (**b**), $Fe_{3-x}Co_xO_4$ (**f**), and $Fe_{3-x}Ni_xO_4$ (**i**). *Solid lines* represent experimental curves; *dash lines* are fitting curves

curves (Fig. 3c) corresponds to the V–O shell distribution (Zhang et al. 2011). The V–O bond length in the series of $Fe_{3-x}V_xO_4$ is close to that in V_2O_3 at about 1.6 Å (Fig. 3c). This suggests that the V–O coordination shell in $Fe_{3-x}V_xO_4$ is the same as that in V_2O_3, being identifiable as $V(III)O_6$. The second peak in the FT curve is a doublet, related to the V–V/Fe_{oct} and V–Fe_{tet} shell distributions (Zhang et al. 2011). As the V content increases, the intensity of the latter component decreases, indicating less static disorder (Choi et al. 2002).

The fitted EXAFS and FT results are also shown in Fig. 3e, f, while the fitted parameters are listed in Table 2. The distances of the first-nearest V–O shells for $Fe_{2.84}V_{0.16}O_4$, $Fe_{2.74}V_{0.26}O_4$, and $Fe_{2.66}V_{0.34}O_4$ are 2.03 ± 0.01, 1.99 ± 0.01, and 1.99 ± 0.01 Å, respectively, consistent with the value for $V(III)O_6$. For $Fe_{2.84}V_{0.16}O_4$, the next nearest coordination V–V/Fe shell shows three distances at 3.00 ± 0.02, 3.46 ± 0.02, and 5.21 ± 0.04 Å. These values are consistent with the Fe_{oct}–Fe_{oct}/Fe_{tet} distances of 2.97, 3.48, and 5.14 Å for magnetite without substitution (Fe_3O_4), indicating that V^{3+} occupies the octahedral sites in magnetite structure (Fig. 4a). The discussion for Fe K-edge Fourier transform of EXAFS spectra is shown in Text A1 and Fig. A1.

The coordination number of V–V/Fe shells is low in comparison with the theoretical value for magnetite (Table 2). The difference becomes more pronounced as the V content of the samples increases. The peak at 4.5–6.0 Å in the FT curves of $Fe_{3-x}V_xO_4$ (Fig. 3c) may be ascribed to the linear single-scattering and multiple-scattering of V, arising from metal atom arrangement in closest-packed and edge-shared octahedral sites (Pandya 1994), as modeled in Fig. 4b. Because of the high symmetry, the distances from the central vanadium atom (A0) to the first-nearest vanadium atoms (A1), and the next nearest atoms (A2), are in the range of 2.5–3.0 and 4.5–6.5 Å, respectively. Scattering results from the overlaying of two-, three-, and four-leg scattering paths whose total distance is in the range

Table 2 EXAFS fitting results for $Fe_{3-x}V_xO_4$ samples (*R*-factor = 0.01)

Sample	$Fe_{2.84}V_{0.16}O_4$			$Fe_{2.74}V_{0.26}O_4$			$Fe_{2.66}V_{0.34}O_4$		
	N[a]	R (Å)[b]	σ^2 (Å^2)[c]	N	R (Å)	σ^2 (Å^2)	N	R (Å)	σ^2 (Å^2)
V–O	5.2 (5)	2.03 (1)	0.004 (1)	5.1 (5)	1.99 (2)	0.004 (1)	5.0 (5)	1.99 (1)	0.004 (1)
V–V/Fe	5.3 (9)	3.00 (2)	0.008 (3)	5.1 (8)	3.00 (2)	0.008 (2)	5.1 (9)	3.02 (2)	0.007 (2)
V–V/Fe	6 (1)	3.46 (2)	0.006 (2)	6 (1)	3.45 (2)	0.007 (1)	5 (1)	3.48 (3)	0.006 (3)
V–V/Fe	13 (1)	5.21 (4)	0.008 (3)	12 (1)	5.21 (3)	0.010 (2)	11 (1)	5.24 (4)	0.009 (3)

[a] Coordination numbers

[b] Bond lengths

[c] Debye–Waller factors

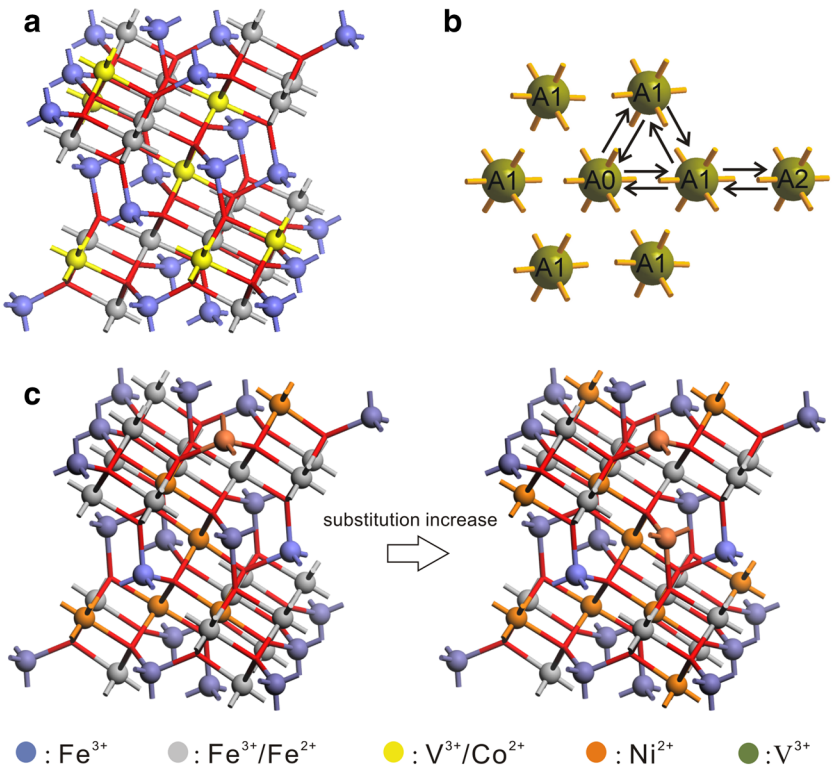

Fig. 4 **a** Atomic model of the $Fe_{3-x}V_xO_4$ and $Fe_{3-x}Co_xO_4$ spinel structure; **b** linear single-scattering and multiple-scattering model for atoms located in closest-packed and edge-shared octahedral positions; and **c** atomic model of the $Fe_{3-x}Ni_xO_4$ spinel structure

of 11.0–12.0 Å, e.g., A0 → A1 → A0 → A1 → A0, A0 → A1 → A1 (another adjacent atom) → A1 → A0, A0 → A1 → A2 → A1 → A0, A0 → A2 → A1 → A0, and A0 → A1 → A2 → A0.

The EXAFS spectra and corresponding FT curves for $Fe_{3-x}Co_xO_4$ are shown in Fig. 3e, f, respectively. The position of first peak in the FT curves for $Fe_{3-x}Co_xO_4$ is close to that for CoO, suggesting that the Co–O bond length of $Fe_{3-x}Co_xO_4$ is similar to that of CoO in octahedral Co(II)O_6 at about 1.6 Å (Fig. 3f; Vaingankar et al. 1980). As for the $Fe_{3-x}V_xO_4$ series, the doublet is ascribable to two different distances of Co–Co/Fe shells. For $Fe_{2.80}Co_{0.20}O_4$, $Fe_{2.57}Co_{0.43}O_4$, and $Fe_{2.33}Co_{0.67}O_4$, the distances of Co–O shells are 2.04 ± 0.01, 2.05 ± 0.01, and 2.06 ± 0.01 Å, respectively (Table 3), consistent with the Co–O coordination of octahedral Co(II)O_6. The Co–O bond length in $Fe_{3-x}Co_xO_4$ is larger than the V–O bond length in $Fe_{3-x}V_xO_4$, because the radius of Co^{2+} (75 pm) is larger than that of V^{3+} (65 pm). For $Fe_{2.80}Co_{0.20}O_4$, the Co–Co/Fe shells also have three distances, namely 2.98 ± 0.02, 3.46 ± 0.02, and 5.17 ± 0.04 Å. The Co–Co/Fe distances are identical to the Fe_{oct}–Fe_{oct}/Fe_{tet} distances in the magnetite structure.

In contrast to $Fe_{3-x}V_xO_4$, the coordination number of the Co–Co/Fe shell in $Fe_{3-x}Co_xO_4$ is higher than the theoretical value, especially for the samples with high cobalt content. A peak also appears around 5.5 Å, due to the linear single-scattering and multiple-scattering among Co atoms located in closest-packed and edge-shared octahedral sites.

The EXAFS spectra (Fig. 3h) for $Fe_{3-x}Ni_xO_4$ resemble those for $Fe_{3-x}Co_xO_4$ (Fig. 3e), although some differences are noticeable in the high k range. The oscillation at 9.5 $Å^{-1}$ in the spectrum of $Fe_{2.29}Ni_{0.71}O_4$ is sharper than those in the spectra of $Fe_{2.52}Ni_{0.48}O_4$ and $Fe_{2.76}Ni_{0.24}O_4$, and a new oscillation appears at about 10.5 $Å^{-1}$ (Fig. 3h). The EXAFS spectrum of $Ni(OH)_2$ also displays this special character. This may suggest that the structural environment of Ni in $Fe_{3-x}Ni_xO_4$ resembles that in $Ni(OH)_2$ as the nickel content increases. In the FT curves for $Fe_{3-x}Ni_xO_4$, the first peak near 1.5 Å is similar to that for $Ni(OH)_2$ (Fig. 3i). A doublet appears in the region of 2.0–3.5 Å, due to the overlapping contribution from Ni–Ni/Fe shells. With the increase in Ni content, the first peak of the doublet weakens greatly. Interestingly, the position of the first peak is close to that observed for $Fe_{3-x}V_xO_4$ and $Fe_{3-x}Co_xO_4$, while the distance of the second component is close to that of $Ni(OH)_2$ contributed by Ni–Ni shells.

From this analysis, we infer that the nickel cation in the $Fe_{3-x}Ni_xO_4$ structure may occurs in two different coordination states. One of these corresponds to Ni substituting for octahedral Fe in the bulk structure of magnetite, while the other represents octahedral coordinated Ni exposed on the magnetite surface and bound to hydroxyl radicals (Fig. 4c). As the Ni content in the samples increases, the structural environment of Ni become similar to that of Ni in $Ni(OH)_2$. Since the two coordination states of Ni could hardly be differentiated by EXAFS, difference in fitting the EXAFS spectra had been neglected. The distances of Ni–O shells for $Fe_{2.76}Ni_{0.24}O_4$, $Fe_{2.52}Ni_{0.48}O_4$, and $Fe_{2.29}Ni_{0.71}O_4$ are 2.05 ± 0.01, 2.05 ± 0.01, and 2.06 ± 0.01 Å, respectively (Table 4). These values lie between the theoretical value of octahedral Ni in bulk magnetite (2.02 Å) and that of octahedral Ni in $Ni(OH)_2$ (2.09 Å). The Ni–Ni/Fe distances in $Fe_{2.76}Ni_{0.24}O_4$ of 2.93 ± 0.02, 3.10 ± 0.04, 3.44 ± 0.03, and 5.08 ± 0.05 Å are also close to the Fe_{oct}–Fe_{oct}/Fe_{tet} distances in magnetite (2.97, 3.48, and 5.14 Å), and the Ni–Ni distance (3.05 Å) in $Ni(OH)_2$. For the Ni–Ni/Fe bond, with the increase in Ni content, the coordination number

Table 3 EXAFS fitting results for $Fe_{3-x}Co_xO_4$ (R-factor = 0.01)

Sample	$Fe_{2.80}Co_{0.20}O_4$			$Fe_{2.57}Co_{0.43}O_4$			$Fe_{2.33}Co_{0.67}O_4$		
	N	R (Å)	σ^2 (Å^2)	N	R (Å)	σ^2 (Å^2)	N	R (Å)	σ^2 (Å^2)
Co–O	5.2 (5)	2.04 (1)	0.004 (1)	5.7 (6)	2.05 (1)	0.009 (2)	5.3 (7)	2.06 (1)	0.009 (3)
Co–Co/Fe	6.7 (8)	2.98 (2)	0.008 (3)	6.9 (9)	2.98 (2)	0.011 (2)	6.9 (9)	2.98 (2)	0.011 (2)
Co–Co/Fe	6 (1)	3.46 (2)	0.006 (2)	6 (1)	3.45 (2)	0.008 (2)	6 (1)	3.46 (3)	0.009 (2)
Co–Co/Fe	13 (1)	5.17 (4)	0.008 (3)	14 (1)	5.18 (3)	0.009 (2)	14 (1)	5.19 (3)	0.010 (2)

The notations N, R, and σ^2 have the same meaning as for Table 2

Table 4 EXAFS fitting results for $Fe_{3-x}Ni_xO_4$ (R-factor = 0.02)

Sample	$Fe_{2.76}Ni_{0.24}O_4$			$Fe_{2.52}Ni_{0.48}O_4$			$Fe_{2.29}Ni_{0.71}O_4$		
	N	R (Å)	σ^2 (Å^2)	N	R (Å)	σ^2 (Å^2)	N	R (Å)	σ^2 (Å^2)
Ni–O	6.0 (7)	2.05 (1)	0.006 (1)	6.1 (8)	2.05 (1)	0.006 (2)	5.9 (7)	2.06 (1)	0.006 (2)
Ni–Ni/Fe	2.9 (8)	2.93 (2)	0.007 (4)	2.8 (8)	2.94 (2)	0.006 (4)	2.4 (8)	2.93 (2)	0.009 (4)
Ni–Ni/Fe	2.9 (8)	3.44 (3)	0.013 (6)	2.8 (8)	3.44 (3)	0.013 (6)	2.4 (8)	3.44 (3)	0.011 (6)
Ni–Ni/Fe	5.8 (8)	5.08 (5)	0.009 (5)	5.6 (8)	5.09 (5)	0.009 (5)	4.9 (8)	5.08 (5)	0.010 (5)
Ni–Ni	3.1 (8)	3.10 (4)	0.006 (3)	3.2 (9)	3.10 (4)	0.006 (3)	3.6 (9)	3.09 (4)	0.006 (3)

The notations N, R, and σ^2 have the same meaning as for Table 2

decreases from 2.9 to 2.4 and from 5.8 to 4.9, while for the Ni–Ni bond, the coordination number increases from 3.1 to 3.6. The Ni–Ni/Fe bond is fitted by the octahedral Ni in bulk magnetite, while the Ni–Ni bond is fitted by the octahedral Ni in $Ni(OH)_2$. Such changes in the coordination number indicate that the occupancy of Ni in octahedral sites on magnetite surface increases. The surface Ni cations need to adsorb the hydroxyls in the aqueous solution to keep the charge equilibrium, which makes structural environment of Ni similar to that of Ni in $Ni(OH)_2$. Furthermore, the peak related to the linear single-scattering and multiple-scattering among Ni located in closest-packed and edge-shared octahedral sites also intensifies (Fig. 3i). As the distribution of Ni^{2+} cations on the octahedral sites of magnetite surface increases, the crystallinity decreases (Fig. 1c), and the SSA of magnetite accordingly increases (Table 1). But the increase in SSA is also related to the magnesium decrease and the resultant decrease in aggregation by Ni^{2+} substitution, which has been indicated in the previous study (Costa et al. 2006).

From the XAFS analysis, V^{3+}, Co^{2+}, and Ni^{2+} cations occupy octahedral sites in the spinel structure of magnetite, which is consistent with the Mössbauer spectroscopy results in the previous study (Costa et al. 2006; Liang et al. 2010). But XAFS analysis not only provides the information about the valence, coordination number, and coordination shell distances of the substituting cations, but also distinguishes the occupation sites between bulk structure and the surface of magnetite.

Crystal-field theory analysis

The occupancy by V, Co, and Ni of structural sites can be explained by crystal-field theory (CFT). The spinels are a group of minerals with the general formula of AB_2O_4 where A and B denote transition metals. The *d*-orbital-based CFT facilitates the computation of octahedral site preference energy (*OSPE*) for both A and B cations. The *OSPE* is the difference between the crystal-field stabilization energy (*CFSE*) for octahedral and tetrahedral coordination. The *OSPE* values for common transition metal cations are shown in Table 5 (Mcclure 1957; Dunitz and Orgel 1957). Cations with a high *OSPE* have preferential entry into octahedral sites. Since the *OSPE* of Fe^{2+} is larger than that of Fe^{3+}, the octahedral sites in the spinel structure of magnetite are occupied by Fe^{2+}, whereas both octahedral and tetrahedral sites may be occupied by Fe^{3+}. Since all three metal cations (V^{3+}, Co^{2+}, and Ni^{2+}) have a larger *OSPE* than either Fe^{2+} or Fe^{3+}, they would preferentially occupy octahedral sites in the spinel structure, in accordance with the results of XAFS analysis.

Effects on physicochemical properties

The substitution of transition metals greatly affects the physicochemical properties and reactivity of magnetites. Herein, the obtained results about valence and site occupancy of the substituting cations (V^{3+}, Co^{2+}, and Ni^{2+}) were used to discuss their effect on the properties of magnetite.

From the previous studies (Liang et al. 2010, 2013b), V^{3+} has a negative effect on the thermal stability of spinel structure, while Co^{2+} and Ni^{2+} show a positive effect (Fig. A2), which has been verified in this study. For magnetite without substitution, its calcined products at 800 °C were composed of hematite. When Co- and Ni-substituted magnetites were calcined, the Co^{2+} and Ni^{2+} cations combined with Fe^{3+} to form spinel $CoFe_2O_4$ and $NiFe_2O_4$. But for V-substituted magnetite, after calcination, it was changed to be the composition of V_2O_5 and hematite. From the previous research (Sarda and Rousset 1993), the phase transformation from maghemite (γ-Fe_2O_3) to hematite (α-Fe_2O_3) corresponds to a lattice rearrangement, which takes place by relative sliding of the atomic layers and breaking of several Fe–O bonds. The effect of metal substitution on the thermal stability of maghemite can be explained by this mechanism. The valence of Ni and Co is +2, which was stable under the calcination at 800 °C, so Ni^{2+} and Co^{2+} stayed in the spinel structure with Co/Ni–O bond and formed their ferrites with Fe^{3+}. For V series, the presence of V_2O_5 in the calcined products is ascribed to the oxidation of V^{3+} to V^{5+}, which was not tolerated in the magnetite structure, due to the high valence and small radius of V^{5+}. The oxidation of V^{3+} to V^{5+} was in the temperature range of 300–400 °C, which broke the V/Fe–O bonds, and decreased the temperature of phase transformation maghemite–hematite.

Ni^{2+} substitution in magnetite greatly increases the concentration of surface hydroxyl groups, while the V^{3+} and

Table 5 *d*-orbital electron configuration and OSPE values for some transition metal cations (Mcclure 1957)

Cation	$3d^n$	Electron configuration	$(CFSE)_{OCT}$ (KJ/mol)	$(CFSE)_{TET}$ (KJ/mol)	OSPE (KJ/mol)
V^{3+}	d^2	$(t_{2g})^2(e_g)^0$	−160.2	−106.7	−53.5
Fe^{3+}	d^5	$(t_{2g})^3(e_g)^2$	0	0	0
Fe^{2+}	d^6	$(t_{2g})^4(e_g)^2$	−49.8	−33.1	−16.7
Co^{2+}	d^7	$(t_{2g})^5(e_g)^2$	−92.9	−61.9	−31.0
Ni^{2+}	d^8	$(t_{2g})^6(e_g)^2$	−122.2	−36.0	−86.2

CFSE crystal-field stabilization energy, *OSPE* octahedral site preference energy

Co^{2+} do not show such effect (Liang et al. 2013b). EXAFS analysis suggests that a proportion of the incorporated Ni^{2+} cations occupy octahedral sites on the magnetite surface. The Ni^{2+} cations exposed at surface sites of magnetite can coordinate OH^- groups, enhancing the capacity of magnetite for taking up anionic species by legend exchange and cationic on by complexation. For Co^{2+} and V^{3+}, they mainly occupied the bulk structure by substituting Fe^{2+} and Fe^{3+}, respectively, without obvious increase in surface hydroxyl amount on the magnetite surface.

The presence of V^{3+} and Co^{2+} in the structure of magnetite enhances the catalytic activity of the mineral in heterogeneous Fenton reaction (Figs. A3 and A4) (Liang et al. 2010; Zhong et al. 2014). The heterogeneous Fenton reaction follows the hydroxyl radical-mediated mechanism, in which hydroxyl radicals ($^{\cdot}OH$) are generated by the reaction between H_2O_2 and catalyst (Maezono et al. 2011; Zhang et al. 2009). Fe^{2+} is the most active cation (Anipsitakis and Dionysiou 2004). The high Fenton reactivity of magnetite originates from the presence of Fe^{2+} in the spinel structure, and the occupancy of Fe^{2+} and Fe^{3+} on the octahedral sites (Eqs. 1, 2). The electron transfer between the iron species allows the regeneration of Fe^{2+} (Costa et al. 2006). From the XAFS characterization, V and Co are in the valence of +3 and +2, respectively, and occupy the octahedral sites in the magnetite structure. Both cations promote the electron transfer between the redox pairs V^{3+}/V^{4+} or Co^{2+}/Co^{3+} with Fe^{2+}/Fe^{3+} for the generation of active sites and hence enhances the catalytic activity of magnetite.

$$\equiv Fe^{3+}_{surf} + H_2O_2 \rightarrow \equiv Fe^{2+}_{surf} + {}^{\cdot}OOH + H^+ \quad (1)$$

$$\equiv Fe^{2+}_{surf} + H_2O_2 \rightarrow \equiv Fe^{3+}_{surf} + {}^{\cdot}OH + H^+ \quad (2)$$

For Ni^{2+}, though it inhibited Fenton activity of magnetite (Fig. A4), it improved the reactivity of magnetite toward Oxone activation (Fig. A5). This was due to the higher activity of Ni^{2+} than Fe^{2+} or Fe^{3+} in $KHSO_5$ decomposition and inert performance in H_2O_2 decomposition (Anipsitakis and Dionysiou 2004). From the XAFS results, Ni concentrated on the octahedral sites of magnetite surface with the substitution increase. The increase in active sites on the magnetite surface leads to an improvement of the activity toward Oxone activation.

Conclusions

The valence and local atomic environment of V, Co, and Ni in substituted magnetites were investigated in this study. XANES indicates that the valence of these cations is +3, +2, and +2, respectively. Consistent with crystal-field theory calculations, EXAFS analysis suggests that V^{3+} and Co^{2+} as well as Ni^{2+} (in part) are incorporated into magnetite by substituting for octahedral Fe in the bulk structure of the mineral. A proportion of the incorporated Ni^{2+} cations occupy octahedral sites on the surface of magnetite. The valence of the substituting cations, and their location in the structure, affects the physicochemical properties and surface reactivity of magnetite. The present investigation provides insight into the structure of transition metal-substituted magnetites and their potential applications in industry and catalysis.

Acknowledgments We gratefully acknowledge Beijing Synchrotron Radiation Facility (BSRF) for providing us the beam time for the XAFS measurement. We gratefully acknowledge the National Natural Science Foundation of China (Grant Nos. 41172045 and 41302026) and Natural Science Foundation of Guangdong Province, China (Grant No. S2012010009598) for financial support. This is contribution No. IS-1990 from GIG CAS.

References

Anipsitakis GP, Dionysiou DD (2004) Radical generation by the interaction of transition metals with common oxidants. Environ Sci Technol 38(13):3705–3712. doi:10.1021/Es035121o

Brabers VAM, Walz F, Kronmuller H (1998) Impurity effects upon the Verwey transition in magnetite. Phys Rev B 58(21):14163–14166. doi:10.1103/PhysRevB.58.14163

Carta D, Mountjoy G, Navarra G, Casula MF, Loche D, Marras S, Corrias A (2007) X-ray absorption investigation of the formation of cobalt ferrite nanoparticles in an aerogel silica matrix. J Phys Chem C 111(17):6308–6317. doi:10.1021/Jp0708805

Carta D, Casula MF, Mountjoy G, Corrias A (2008a) Formation and cation distribution in supported manganese ferrite nanoparticles: an X-ray absorption study. Phys Chem Chem Phys 10(21):3108–3117. doi:10.1039/B800359a

Carta D, Loche D, Mountjoy G, Navarra G, Corrias A (2008b) $NiFe_2O_4$ nanoparticles dispersed in an aerogel silica matrix: an X-ray absorption study. J Phys Chem C 112(40):15623–15630. doi:10.1021/Jp803982k

Chen LX, Liu T, Thurnauer MC, Csencsits R, Rajh T (2002) Fe_2O_3 nanoparticle structures investigated by X-ray absorption near-edge structure, surface modifications, and model calculations. J Phys Chem B 106(34):8539–8546. doi:10.1021/Jp025544x

Choi HC, Lee SY, Kim SB, Kim MG, Lee MK, Shin HJ, Lee JS (2002) Local structural characterization for electrochemical insertion-extraction of lithium into CoO with X-ray absorption spectroscopy. J Phys Chem B 106(36):9252–9260. doi:10.1021/Jp0205968

Cornell RM, Schwertmann U (2003) The iron oxides: structure, properties, reactions, occurrences and uses. Wiley, New York

Costa RCC, de Fatima M, Lelis F, Oliveira LCA, Fabris JD, Ardisson JD, Rios RRVA, Silva CN, Lago RM (2003) Remarkable effect of Co and Mn on the activity of $Fe_{3-x}M_xO_4$ promoted oxidation of organic contaminants in aqueous medium with H_2O_2. Catal Commun 4(10):525–529. doi:10.1016/j.catcom.2003.08.002

Costa RCC, Lelis MFF, Oliveira LCA, Fabris JD, Ardisson JD, Rios RRVA, Silva CN, Lago RM (2006) Novel active heterogeneous Fenton system based on $Fe_{3-x}M_xO_4$ (Fe Co, Mn, Ni): the role of M^{2+} species on the reactivity towards H2O2 reactions. J Hazard Mater 129(1–3):171–178. doi:10.1016/j.jhazmat.2005.08.028

Dunitz JD, Orgel LE (1957) Electronic properties of transition-metal oxides-ii: cation distribution amongst octahedral and tetrahedral sites. J Phys Chem Solids 3(3–4):318–323. doi:10.1016/0022-3697(57)90035-5

Dupuis C, Beaudoin G (2011) Discriminant diagrams for iron oxide trace element fingerprinting of mineral deposit types. Miner Depos 46(4):319–335. doi:10.1007/s00126-011-0334-y

Farges F, Munoz M, Siewert R, Malavergne V, Brown GE, Behrens H, Nowak M, Petit PE (2001) Transition elements in water-bearing silicate glasses/melts. Part II. Ni in water-bearing glasses. Geochim Cosmochim Acta 65(10):1679–1693. doi:10.1016/S0016-7037(00)00624-4

Kester E, Gillot B, Perriat P, Dufour P, Villette C, Tailhades P, Rousset A (1996) Thermal behavior and cation distribution of submicron copper ferrite spinels $Cu_xFe_{3-x}O_4$ ($0 \leq x \leq 0.5$) studied by DTG, FtIR, and XPS. J Solid State Chem 126(1):7–14. doi:10.1006/jssc.1996.0302

Kumari N, Kumar V, Singh SK (2014) Synthesis, structural and dielectric properties of Cr^{3+} substituted Fe_3O_4 nano-particles. Ceram Int 40(8):12199–12205

Latta DE, Pearce CI, Rosso KM, Kemner KM, Boyanov MI (2013) Reaction of U-VI with titanium-substituted magnetite: influence of Ti on U-IV Speciation. Environ Sci Technol 47(9):4121–4130. doi:10.1021/Es303383n

Liang XL, Zhu SY, Zhong YH, Zhu JX, Yuan P, He HP, Zhang J (2010) The remarkable effect of vanadium doping on the adsorption and catalytic activity of magnetite in the decolorization of methylene blue. Appl Catal B 97(1):151–159

Liang XL, He ZS, Zhong YH, Tan W, He HP, Yuan P, Zhu JX, Zhang J (2013a) The effect of transition metal substitution on the catalytic activity of magnetite in heterogeneous Fenton reaction: in interfacial view. Colloids Surf A Physicochem Eng Asp 435:28–35. doi:10.1016/j.colsurfa.2012.12.038

Liang XL, Zhong YH, Zhu SY, He HP, Yuan P, Zhu JX, Jiang Z (2013b) The valence and site occupancy of substituting metals in magnetite spinel structure $Fe_{3-x}M_xO_4$ (M = Cr, Mn, Co and Ni) and their influence on thermal stability: an XANES and TG-DSC investigation. Solid State Sci 15:115–122. doi:10.1016/j.solidstatesciences.2012.10.005

Maezono T, Tokumura M, Sekine M, Kawase Y (2011) Hydroxyl radical concentration profile in photo-Fenton oxidation process: generation and consumption of hydroxyl radicals during the discoloration of azo-dye Orange II. Chemosphere 82(10):1422–1430. doi:10.1016/j.chemosphere.2010.11.052

Magalhaes F, Pereira MC, Botrel SEC, Fabris JD, Macedo WA, Mendonca R, Lago RM, Oliveira LCA (2007) Cr-containing magnetites $Fe_{3-x}Cr_xO_4$: the role of Cr^{3+} and Fe^{2+} on the stability and reactivity towards H_2O_2 reactions. Appl Catal A Gen 332(1):115–123. doi:10.1016/j.apcata.2007.08.002

Mcclure DS (1957) The distribution of transition metal cations in spinels. J Phys Chem Solids 3(3–4):311–317. doi:10.1016/0022-3697(57)90034-3

Nohair M, Aymes D, Perriat P, Gillot B (1995) Infrared spectra-structure correlation study of vanadium–iron spinels and of their oxidation-products. Vib Spectrosc 9(2):181–190. doi:10.1016/0924-2031(95)00004-E

Oliveira LCA, Fabris JD, Rios RRVA, Mussel WN, Lago RM (2004) $Fe_{3-x}Mn_xO_4$ catalysts: phase transformations and carbon monoxide oxidation. Appl Catal A Gen 259(2):253–259. doi:10.1016/j.apcata.2003.09.033

Ounnunkad S, Winotai P, Phanichphant S (2006) Cation distribution and magnetic behavior of $Mg_{1-x}Zn_xFe_2O_4$ ceramics monitored by Mossbauer spectroscopy. J Electroceram 16(4):363–368. doi:10.1007/s10832-006-9880-6

Pandya KI (1994) Multiple-scattering effects in X-ray-absorption fine-structure—chromium in a tetrahedral configuration. Phys Rev B 50(21):15509–15515. doi:10.1103/PhysRevB.50.15509

Pantelouris A, Modrow H, Pantelouris M, Hormes J, Reinen D (2004) The influence of coordination geometry and valency on the K-edge absorption near edge spectra of selected chromium compounds. Chem Phys 300(1–3):13–22. doi:10.1016/j.jchemphys.2003.12.017

Pearce CI, Qafoku O, Liu J, Arenholz E, Heald SM, Kukkadapu RK, Gorski CA, Henderson CMB, Rosso KM (2012) Synthesis and properties of titanomagnetite ($Fe_{3-x}Ti_xO_4$) nanoparticles: a tunable solid-state Fe(II/III) redox system. J Colloid Interface Sci 387:24–38. doi:10.1016/j.jcis.2012.06.092

Peterson ML, Brown GE, Parks GA, Stein CL (1997) Differential redox and sorption of Cr(III/VI) on natural silicate and oxide minerals: EXAFS and XANES results. Geochim Cosmochim Acta 61(16):3399–3412. doi:10.1016/S0016-7037(97)00165-8

Ramankutty CG, Sugunan S (2001) Surface properties and catalytic activity of ferrospinels of nickel, cobalt and copper, prepared by soft chemical methods. Appl Catal A Gen 218(1–2):39–51. doi:10.1016/S0926-860x(01)00610-X

Salazar-Alvarez G, Olsson RT, Sort J, Macedo WAA, Ardisson JD, Baro MD, Gedde UW, Nogues J (2007) Enhanced coercivity in Co-rich near-stoichiometric $CoFe_{3-x}O_{4+\delta}$ nanoparticles prepared in large batches. Chem Mater 19(20):4957–4963. doi:10.1021/Cm070827t

Sarda C, Rousset A (1993) Thermal-stability of barium-doped iron-oxides with spinel structure. Thermochim Acta 222(1):21–31. doi:10.1016/0040-6031(93)80535-I

Sickafus KE, Wills JM, Grimes NW (1999) Structure of spinel. J Am Ceram Soc 82(12):3279–3292

Sorescu M, Grabias A, Tarabasanu-Mihaila D, Diamandescu L (2001) From magnetite to cobalt ferrite. J Mater Synth Process 9(3):119–123. doi:10.1023/A:1013241312932

Sorescu M, Grabias A, Tarabasanu-Mihaila D, Diamandescu L (2002) Influence of cobalt and nickel substitutions on populations, hyperfine fields, and hysteresis phenomenon in magnetite. J Appl Phys 91(10):8135–8137. doi:10.1063/1.1456436

Su SN, Guo WL, Leng YQ, Yi CL, Ma ZM (2013) Heterogeneous activation of Oxone by $Co_xFe_{3-x}O_4$ nanocatalysts for degradation of rhodamine B. J Hazard Mater 244:736–742. doi:10.1016/j.jhazmat.2012.11.005

Vaingankar AS, Khasbardar BV, Patil RN (1980) X-ray spectroscopic study of cobalt ferrite. J Phys F Met Phys 10(7):1615–1619. doi:10.1088/0305-4608/10/7/027

Varshney D, Yogi A (2010) Structural and transport properties of stoichiometric and Cu^{2+}-doped magnetite: $Fe_{3-x}Cu_xO_4$. Mater Chem Phys 123(2–3):434–438. doi:10.1016/j.matchemphys.2010.04.036

Waychunas GA, Apted MJ, Brown GE (1983) X-ray K-edge absorption-spectra of Fe minerals and model compounds: near-edge structure. Phys Chem Miner 10(1):1–9. doi:10.1007/Bf01204319

Zhang H, Fu H, Zhang DB (2009) Degradation of CI acid Orange 7 by ultrasound enhanced heterogeneous Fenton-like process. J Hazard Mater 172(2–3):654–660. doi:10.1016/j.jhazmat.2009.07.047

Zhang MY, Pan G, Zhao DY, He GZ (2011) XAFS study of starch-stabilized magnetite nanoparticles and surface speciation of arsenate. Environ Pollut 159(12):3509–3514. doi:10.1016/j.envpol.2011.08.017

Zhao R, Jia K, Wei JJ, Pu JX, Liu XB (2010) Hierarchically nanostructured Fe_3O_4 microspheres and their novel microwave electromagnetic properties. Mater Lett 64(3):457–459. doi:10.1016/j.matlet.2009.11.043

Zhong YH, Liang XL, He ZS, Tan W, Zhu JX, Yuan P, Zhu RL, He HP (2014) The constraints of transition metal substitutions (Ti, Cr, Mn, Co and Ni) in magnetite on its catalytic activity in heterogeneous Fenton and UV/Fenton reaction: from the perspective of hydroxyl radical generation. Appl Catal B Environ 150:612–618. doi:10.1016/j.apcatb.2014.01.007

Zhu HY, Zhang S, Huang YX, Wu LH, Sun SH (2013) Monodisperse $M_xFe_{3-x}O_4$ (M = Fe, Cu Co, Mn) nanoparticles and their electrocatalysis for oxygen reduction reaction. Nano Lett 13(6):2947–2951. doi:10.1021/Nl401325u